The Development of a Compact Positron Tomograph for Prostate Imaging

J. S. Huber, *Member, IEEE,* J. Qi, *Member, IEEE,* S. E. Derenzo, *Fellow, IEEE,* W. W. Moses, *Senior Member, IEEE,* R. H. Huesman, *Fellow, IEEE,* and T. F. Budinger, *Member, IEEE*

Abstract—We give design details and expected image results of a compact positron tomograph designed for prostate imaging that centers a patient between a pair of external curved detector banks (ellipse: 45 cm minor, 70 cm major axis). The bottom bank is fixed below the patient bed, and the top bank moves upward for patient access and downward for maximum sensitivity. Each bank is composed of two rows (axially) of 20 CTI PET Systems HR+ block detectors, forming two arcs that can be tilted to minimize attenuation. Compared to a conventional PET system, our camera uses about one-quarter the number of detectors and has almost two times higher solid angle coverage for a central point source, because the detectors are close to the patient. The detectors are read out by modified CTI HRRT data acquisition electronics. The individual detectors are angled in the plane to point towards the prostate to minimize resolution degradation in that region. Inter-plane septa extend 5 cm beyond the scintillator crystals to reduce random and scatter backgrounds. Average- to large-size patients will not be fully encircled by detector rings, causing incomplete sampling due to the side gaps. Monte Carlo simulations (including 20% randoms and 30% scatter fractions) demonstrate the feasibility of detecting and differentiating prostate tumors with a tumor to background ratio of 2:1, using a number of counts that should be achievable with a 6 minute scan after a 10 mCi injection (*e.g.*, carbon-11 choline). Simulations also predict minimal blurring in the 10 cm diameter central region for a wide range of patient sizes.

I. Introduction

We present the development of a compact positron tomograph optimized to image the prostate. This instrument images radiopharmaceuticals that specifically localize in the prostate to confirm the presence, absence or progression of disease. It has approximately four times fewer detectors than a conventional whole-body positron emission tomograph (PET), which will reduce the cost and increase clinical availability.

Prostate cancer has a prevalence and diagnostic rate similar to breast cancer, with 360,000 new cases diagnosed each year and two million men affected by the disease in the United States. Prostate cancer suspicion is typically based on an elevated prostate-specific antigen (PSA) level or a suspicious node found during a digital rectal exam. Serum PSA values do not always correlate well with clinical diagnosis or outcomes [1-3]. Palpation is subjective, insensitive and inexact; more than half of all cancers detected today are not palpable. Treatment decision is based mainly on biopsy confirmation of prostate cancer, but the diagnostic accuracy of prostate biopsies is problematic. Typical treatment options include radical prostatectomy, external beam irradiation, brachytherapy (interstitial implantation of radioactive seeds), androgen ablation (hormone) therapy, or "watchful waiting." A major problem with prostatic cancer therapy is the question of when to treat or whether to treat at all. This is particularly problematic in the case of an increased PSA level with non-diagnostic repeated biopsies or after a prostatectomy. A new imaging technology for sensitive detection of early stage prostate cancer is needed to confirm initial diagnosis and help guide treatment decisions. In addition, a new method is needed to assess response shortly after treatment intervention.

In order to help meet these needs, we are building a compact PET camera optimized to image the prostate. Functional PET imaging will help detect malignant tumors in the prostate and/or prostate bed to confirm an elevated PSA level, as well as possibly help determine tumor "aggressiveness" based on metabolic uptake levels, in order to help guide whether to treat suspected prostatic cancer. Although not optimized to detect distant metastatic disease, this compact PET camera should also image local spread beyond the prostate bed to help guide treatment decisions such as whether a narrow or wide irradiation treatment field is needed.

Promising PET radiopharmaceuticals have recently demonstrated outstanding results in the sensitive detection of prostate cancer, inspiring a new interest in using PET for prostate cancer imaging. Consistent with the evidence of increased pool size of choline in prostate cancer [4, 5], Hara and co-workers demonstrated prostate tumor uptake by [^{11}C]choline. They find that: [^{11}C]choline clears the blood faster than FDG; its uptake in prostate tumors is significantly higher than in normal and surrounding tissues [6, 7], providing excellent tumor/normal contrast; and bladder accumulation is minimal if the correct time course is chosen [8] which is a major advantage over FDG. Additionally, they observe that [^{11}C]choline PET is more sensitive for detecting bone metastases than bone scintigraphy. Therefore,

Manuscript received December 10, 2002. This work was supported in part by the Director, Office of Science, Office of Biological and Environmental Research, Medical Science Division of the U.S. Department of Energy under Contract No. DE-AC03-76SF00098 and in part by Department of Defense grant number DAMD17-02-1-0081.

J. S. Huber, J. Qi, S. E. Derenzo, W. W. Moses, R. H. Huesman and T. F. Budinger are with the Lawrence Berkeley National Laboratory, Mailstop 55-121, 1 Cyclotron Road, Berkeley, CA 94720 USA (telephone: 510-486-6445, e-mail: jshuber@lbl.gov).

[^{11}C]choline is an attractive PET tracer for imaging primary and metastatic tumors of the prostate and potentially for other regions of the body [9-13]. Fig. 1 shows a [^{11}C]choline image of prostate cancer before and after therapy, demonstrating the ability to detect prostate carcinoma using choline and possibly its analogs. Other ^{11}C radiopharmaceuticals are also under investigation for prostate cancer PET imaging, including [^{11}C]acetate and [^{11}C]methionine.

^{18}F imaging has the advantage of a longer half-life, which increases clinical viability since an on-site cyclotron facility would not be necessary (as it would for ^{11}C imaging). Many groups have shown that PET imaging with [^{18}F]fluorodeoxyglucose (FDG) is not a good technique for prostate cancer diagnosis, because FDG is not very prostate specific (with a SUV of typically ~2) and the uptake is overcome by background primarily due to bladder accumulation. The SUV (standard uptake value) is the ratio of activity in the target tissue to the average activity in the body. However, there are several other ^{18}F radiopharmaceuticals currently under investigation for prostate cancer imaging, including [^{18}F]fluorocholine (FCH) [14, 15]. PET images using [^{18}F]fluorocholine demonstrate high standardized uptake values (*e.g.*, SUV of 8), indicating that FCH is well localized in the prostate cancer and can be imaged with good resolution if a short scan time (~five minutes) is used. Therefore, [^{18}F]fluorocholine is also an attractive PET tracer for imaging primary and metastatic tumors of the prostate.

II. Camera Design

A. Overview

These new prostate tracers have motivated us to build a low cost PET camera optimized to image the prostate. Coincidence imaging of positron emitters is achieved using a pair of external curved detector banks, one placed above and one below the patient. Fig. 2 shows the transaxial and sagittal views of the camera. The bottom bank is fixed below the patient bed, and the top bank moves upward for patient access and downward for maximum sensitivity. Each bank consists of two axial rows of 20 CTI ECAT HR+ block detectors, forming two arcs with a minor axis of 45 cm and major axis of 70 cm. Our prostate camera has about one-fourth the number of detectors as in a conventional PET system because: (a) the patient is not fully encircled in 2D, (b) an elliptical shape is used instead of a circular one, and (c) the axial coverage is only 8 cm. However, since the average distance to the detectors is approximately one-half that of a conventional 2D PET system, the solid angle for a central source is approximately double for average-sized men. Thus, we expect to achieve improved detection efficiency at a lower cost.

Individual detector modules are angled to point towards the camera center near the prostate location in order to reduce penetration effects (in the detector) for annihilation photons originating in the prostate. This increases resolution selectively in the region of the prostate and is an unique feature for a non-circular camera geometry. Annihilation photons from other parts of the field of view (FOV) will suffer increased penetration effects, but these FOV regions are less important. Both detector banks can be tilted to image the prostate while minimizing attenuation (*i.e.*, above the buttocks and below the stomach, see Fig. 2), but the gantry allows zero tilt for thin patients. A patient of average size is not fully encircled in 2D, which results in irregular and incomplete sampling due to the side gaps. Despite this incomplete sampling, we are able to reconstruct nearly artifact free images in the region of interest by using an iterative reconstruction algorithm [16].

The camera design also includes shielding [16]. Inter-plane septa extend 5 cm beyond the scintillator crystals to reduce background events from random coincidences and from photons that Compton scatter in the patient. Lead shields are also used on the ends to reduce activity from outside the field of view.

B. Electronics

Our camera uses modified commercial components in a novel geometry. We are using 80 CTI ECAT HR+ block detectors that are three attenuation lengths thick for good detection efficiency with narrow detector elements (*i.e.*, 8 x 8 arrays of 4.5 x 4.5 x 30 mm^3 BGO crystals) to achieve good spatial resolution. We are using modified front end, coincidence, and readout electronics developed by CTI for the HRRT brain imaging PET camera, as shown in Fig. 3. Since we are creating a non-standard camera with HR+ and HRRT components, a custom conversion board is necessary. Events are detected and assigned an arrival time, the crystal of interaction is identified, energy qualification is performed, and a digital word is formed using 28 CTI HRRT Analog Subsection boards. The output signals from the Analog Subsection boards are then multiplexed by six custom Detector Head Interface (DHI) boards, which are based on the CTI HRRT DHI design but each services a maximum of 15 (rather than 117) detector modules. We are using six DHI boards to allow coincidences between detector modules within the same bank and plane. A CTI Coincidence Processor identifies singles events in the different DHI boards that are in coincidence, and the output is sent to a Pentium-based computer system that accumulates the coincident data, reconstructs the images, and displays them.

We previously reported on the conceptual design of this prostate camera [16]. We have moved from the idea stage into the building stage. We have acquired all HR+ detector blocks and electronics boards. We are currently testing the CTI electronics and modifying the DAQ software for our system.

C. Gantry

The gantry and electronic housing is designed and under construction. We still need to design and build the septa and patient bed. Fig. 4 shows a photograph of the top and bottom aluminum arc plates with some of the CTI ECAT HR+ detector modules mounted in place. The detector

modules are individually positioned to point towards the center of the camera, as discussed in Section IIA.

Fig. 5 shows a 3-D drawing of the camera with many of the gantry and electronic housing details. The upper bank is mounted onto a main aluminum back-plate in order to control the vertical motion using a hand-crank, allowing upward movement for patient access and downward to maximize sensitivity. A second hand-crank is used to adjust the overall tilt of both upper and lower banks. The near end of Fig. 5 also shows the electronic housing. The six DHI boards are mounted horizontally to the housing that holds their corresponding Analog Subsection boards. The Coincidence Processor board is mounted onto the cabinet door for compactness. The ±5V and high voltage power supplies are mounted on the far end.

III. Expected Performance

A. Point Source Grid

To determine the size of the region of high spatial resolution, we have performed statistical noise-free simulations. Fig. 6 shows reconstructed point sources in a grid. Data are generated with interactions throughout the crystal, assuming an attenuation length of 10 mm in the BGO crystal. A preliminary iterative maximum likelihood algorithm is used in the reconstruction without correcting for detector penetration. The point sources are 5 cm apart, and the grid covers the majority of the field of view. All point sources are clearly visible in the image (black = high uptake). As expected, increased radial blurring due to penetration effects is seen in the region representing the outer edge of the patient. Since we are optimizing resolution at the center near the prostate at the price of resolution at the edges, distant metastases will suffer from some resolution degradation. However, good resolution is observed in the 10 cm diameter central region near the prostate. In Fig. 6, the central point has both a radial and tangential fwhm of 2 mm. More representative of the expected spatial resolution, the surrounding eight points have a radial fwhm of 4 mm and tangential fwhm of 3 mm. Improved resolution for more distant points is expected when the reconstruction corrects for detector penetration, although this process increases the statistical noise in the reconstruction.

Assuming that the detector arcs are rigid with a fixed focal spot for each arc, both focal spots are at the center for the 'nominal' gap separation. The above simulation (Fig. 6) assumed this 'nominal' gap distance. In order to investigate the effect of varying the gap between the arcs, the simulation is repeated for a gap range of ±5 cm when the focal spots are no longer in the center. The same minimal blurring within a 10 cm diameter central region is observed for both cases, indicating that a wide range in patient size will not compromise the resolution near the prostate. Fig. 7 shows the reconstructed point source grid with the gap distance increased by +5 cm from 'nominal' position.

The above results show that we can achieve similar resolution in the 10 cm diameter center region as an ECAT HR+ scanner. Using the nominal configuration, we also compute the signal to noise ratio (SNR) of an ideal observer for detecting a small lesion at the grid locations. The background is modeled as an uniform elliptical region (major axis = 40 cm, minor = 30 cm). For the central point, the resulting SNR of the new system is about 27% higher than that of an ECAT HR+ scanner under the same situation, and the SNR is about 20% higher for the surrounding eight points. This indicates that while the resolution is similar, the increase in sensitivity can still improve lesion detection. The above computation is for one 2D direct plane. No random or scattered events are modeled for either scanner.

B. Extended Sources

Monte Carlo methods are used to study the reconstruction of extended sources. Reconstructions are performed with an iterative maximum likelihood technique that assumes statistical noise representing 745 kcounts/slice, a tumor activity concentration that is two times the background activity concentration, 30% scatter fraction, and 20% randoms fraction. The reconstructions are then post-filtered with a very conservative Gaussian function of sigma = 1 pixel = 2 mm. We simulate self-attenuation by assuming a constant attenuation coefficient of 0.0095/mm inside the body. Coincidences between detector modules within the same bank and plane are allowed. Fig. 8(a) shows the body outline of a patient with an extended "prostate" source (2.5 cm diameter circle) with "tumors" in the upper right and lower left quadrants. Fig. 8(b) shows a reconstructed image of the phantom with "tumors" in the upper right and lower left quadrants clearly visible (white = high uptake), demonstrating that we can reconstruct nearly artifact-free images as well as detect and differentiate partial and whole prostate tumors. Our preliminary rate calculations indicate that 745 kcounts per imaging plane will be achievable with a six minute scan after a 10 mCi injection [16]. A relatively short value of six minutes is chosen to demonstrate that good images can be obtained even if the bladder fills rapidly. All published [^{11}C]choline or [^{18}F]fluorocholine studies done to date have used three minutes or longer (up to 30 minutes) imaging times.

C. Data Correction

Our design has sufficient room to incorporate a single photon or positron emitting source for transmission scans, but it would add to the camera cost. We plan to correct without an additional source using calculated attenuation coefficients based on body contours and an uniform attenuation coefficient [16]. Anatomical boundaries can be obtained from the outer edges of emission sinograms acquired from transverse sections [17]. It may also be possible to use heterogeneous attenuation coefficients by identifying tissue types (*e.g.*, soft tissue, bone, and air) based on x-ray CT images.

Because of the unusual geometry of our camera, the sensitivity of each line of response depends on the distance between the two detectors and the face angles of the two detectors; the shorter the distance is, the higher the

sensitivity. Normalization will include geometric correction (sensitivity changes caused by the septa that are not modeled in the solid angle computation), block effect correction, individual detector sensitivity correction, and dead time correction. These factors will be obtained using a scan of an uniform activity plane source such as used in conventional PET scanners. However, because of our specialized geometry and lack of rotational symmetry, the method for deriving the first two factors will be different from that of circular systems and may require a longer scan time to achieve good count statistics.

Random events will be estimated using the delayed window technique. Instead of pre-subtracting histogrammed data, delayed events will be saved in the list mode data stream with a tag to distinguish them from prompt events. For our statistical reconstruction algorithm, the estimated randoms will be included in the forward model in reconstruction.

IV. Discussion

This project is in its initial building phase, so there are many remaining uncertainties, including which radiopharmaceutical will be used, the specific requirements for the radiopharmaceutical and imaging procedure, and the accuracy that physicians would require to perform effective diagnosis and evaluate response to therapy. However, new PET radiopharmaceuticals have recently demonstrated promising results in the sensitive detection of prostate cancer. This PET camera design is also likely to out-perform whole body PET for this task, as the higher sensitivity will help for the short scans that appear to be necessary with choline-like radiopharmaceuticals.

Accurate patient positioning is also critical due to the limited (8 cm) axial extent of the camera. A manually placed external or trans-rectal positron-emitting source could be used to position the prostate near the center of the FOV of the camera. Alternatively, the prostate is visible in ultrasound images acquired with an external transducer, and these images could be used to position the patient bed.

Finally, as Fig. 1 shows, it is difficult to identify features other than the prostate (and possibly the bladder) in the PET images. Local anatomic information is highly desirable to determine the location of the disease within the prostate, as well as to determine whether the disease has spread to the prostate bed. This information could be obtained with dual modality imaging. X-ray CT provides excellent images of the abdomen, but the cost is relatively high. Ultrasound imaging with a trans-rectal probe provides reasonable detail in the region of the prostate and the cost of an ultrasound unit is significantly less than that of a CT imager, so we plan to explore adding co-registered ultrasound imaging capability.

V. Conclusion

Promising new PET tracers for prostate cancer, such as [^{11}C]choline and [^{18}F]fluorocholine, have motivated us to design and build a low cost PET camera optimized for prostate imaging. Monte Carlo simulations demonstrate the feasibility of detecting and differentiating partial and whole prostate tumors with a tumor to background ratio of 2:1, using a six minute scan after a 10 mCi injection. Simulations also predict minimal blurring in the 10 cm diameter central region for a wide range in patient size. Thus, we are currently building a camera that will image prostate tumors with good spatial resolution and image contrast at low cost relative to commercial PET scanners.

VI. Acknowledgment

We thank Dr. Hara from the International Medical Center of Japan for providing the PET images presented in Fig. 1 of this paper. We also thank Dr. Nutt from CPS Innovations for providing detectors and electronics. This work was supported in part by the Director, Office of Science, Office of Biological and Environmental Research, Medical Science Division of the U.S. Department of Energy under Contract No. DE-AC03-76SF00098 and in part by Department of Defense grant number DAMD17-02-1-0081. Reference to a company or product name does not imply approval or recommendation by the University of California or the U.S. Department of Energy to the exclusion of others that may be suitable.

VII. References

1. H. I. Scher and L. W. Chung, "Bone metastases: improving the therapeutic index," *Semin Oncol*, vol. 21, pp. 630-56, 1994.
2. H. I. Scher, M. Mazumdar, and W. K. Kelly, "Clinical trials in relapsed prostate cancer: defining the target," *J Natl Cancer Inst*, vol. 88, pp. 1623-34, 1996.
3. M. A. Eisenberger and W. G. Nelson, "How much can we rely on the level of prostate-specific antigen as an end point for evaluation of clinical trials? A word of caution! [editorial; comment]," *J Natl Cancer Inst*, vol. 88, pp. 779-81, 1996.
4. J. Kurhanewicz, D. B. Vigneron, H. Hricak, et al., "Three-dimensional H-1 MR spectroscopic imaging of the in situ human prostate with high (0.24-0.7-cm3) spatial resolution," *Radiology*, vol. 198, pp. 795-805, 1996.
5. J. Kurhanewicz, D. B. Vigneron, R. G. Males, et al., "The Prostate: Magnetic Resonance Imaging and Spectroscopy: Present and Future," in *Radiologic Clinics of North America*, H. Hricak and P. R. Carroll, Eds. New York, New York: W. B. Saunders Co., 2000, pp. 115-138.
6. T. Hara, N. Kosaka, N. Shinoura, et al., "PET imaging of brain tumor with [methyl-C11]choline," *J Nucl Med*, vol. 38, pp. 842-7, 1997.
7. N. Shinoura, M. Nishijima, T. Hara, et al., "Brain tumors: detection with C-11 choline PET," *Radiology*, vol. 202, pp. 497-503, 1997.
8. T. Hara, N. Kosaka, and H. Kishi, "PET imaging of prostate cancer using carbon-11-choline," *J Nucl Med*, vol. 39, pp. 990-5, 1998.
9. T. Hara, N. Kosaka, T. Kondo, et al., "Imaging of brain tumor, lung cancer, esophagus cancer, colon cancer, prostate cancer, and bladder cancer with [C-11]choline," *J Nucl Med*, vol. 38 (suppl), pp. 250P (abstract), 1997.
10. T. Hara, K. Inagaki, N. Kosaka, et al., "Sensitive detection of mediastinal lymph node metastasis of lung cancer with 11C-choline PET," *J Nucl Med*, vol. 41, pp. 1507-13, 2000.
11. I. J. Jong, T. H. Que, J. Pruim, et al., "Imaging of bladder cancer using carbon-11 choline positron emission tomography," *J. Nucl. Med.*, vol. 41 (5 Suppl), pp. 74, 2000.
12. J. Kotzerke, J. U. Prang, B. Neumaier, et al., "Carbon-11 choline positron emission tomography (PET) of prostate cancer -- first clinical experience," *J. Nucl. Med.*, vol. 41 (5 Suppl), pp. 74, 2000.
13. J. Kotzerke, J. Prang, B. Neumaier, et al., "Experience with carbon-11 choline positron emission tomography in prostate carcinoma," *Eur J Nucl Med*, vol. 27, pp. 1415-9, 2000.
14. T. R. Degrado, R. E. Coleman, S. W. Baldwin, et al., "Fluorine-18 fluorocholine (FCH) as an oncological PET tracer: evaluation in

murine prostate cancer xenograft model," *J. Nucl. Med.*, vol. 41 (5 Suppl), pp. 231, 2000.
15. T. R. Degrado, R. E. Coleman, S. Wang, et al., "Synthesis and Evaluation of F18-labeled Choline as an Oncologic Tracer for Positron Emission Tomography: Initial Findings in Prostate Cancer," *Cancer Research*, vol. 61(1), pp. 110-117, 2001.
16. J. S. Huber, S. E. Derenzo, J. Qi, et al., "Conceptual Design of a Compact Positron Tomograph for Prostate Imaging," *IEEE Trans Nucl Sci*, vol. NS-48, pp. 1506-1511, 2001.
17. T. F. Budinger and G. T. Gullberg, "Three-dimensional reconstruction in nuclear medicine emission imaging," *IEEE Trans Nucl Sci*, vol. NS-21, pp. 2-20, 1974.

Figures:

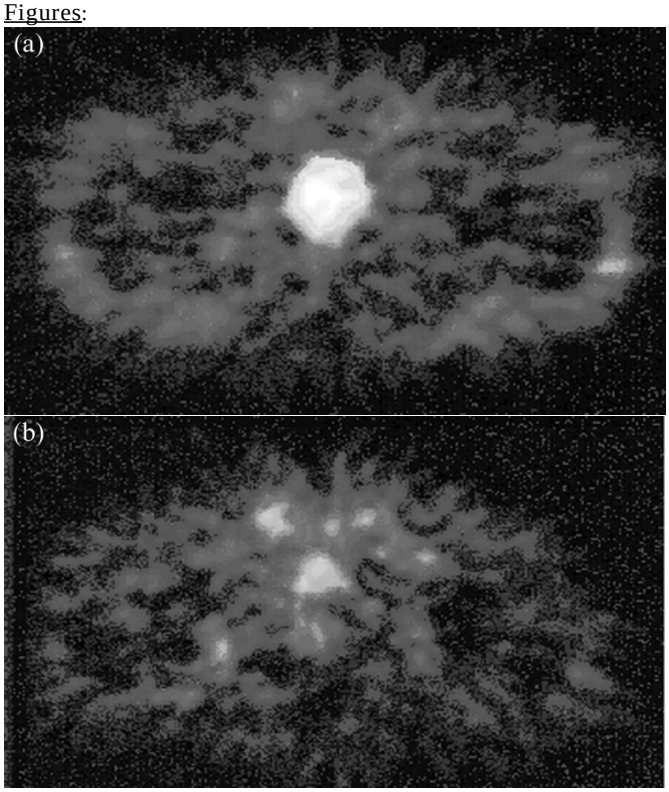

Fig. 1: [^{11}C]choline image of prostate cancer (a) before and (b) after treatment. These grayscale images indicate a high (white) uptake in the prostate cancer compared with a low (gray) uptake elsewhere. Images are provided by Hara and co-workers [8].

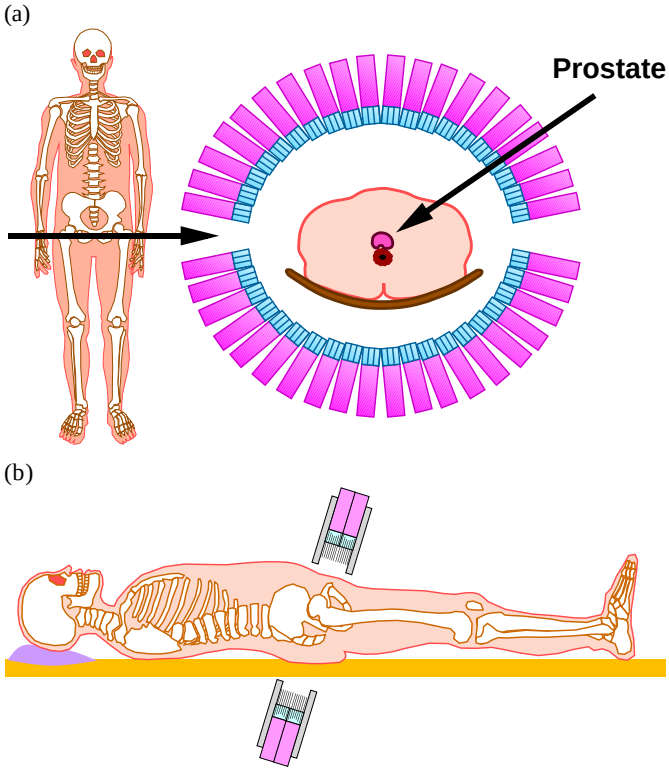

Fig. 2: Positron tomograph for prostate imaging. (a) Drawing of a transaxial view through prostate, showing the patient centered between two detector banks. The individual detector modules are angled to point towards the prostate. (b) Drawing of the sagittal view. The bottom arc is fixed below the patient bed, whereas the top arc adjusts vertically for patient access and compactness. Both detector banks are tilted and positioned as close as possible to the prostate, which improves sensitivity and minimizes attenuation.

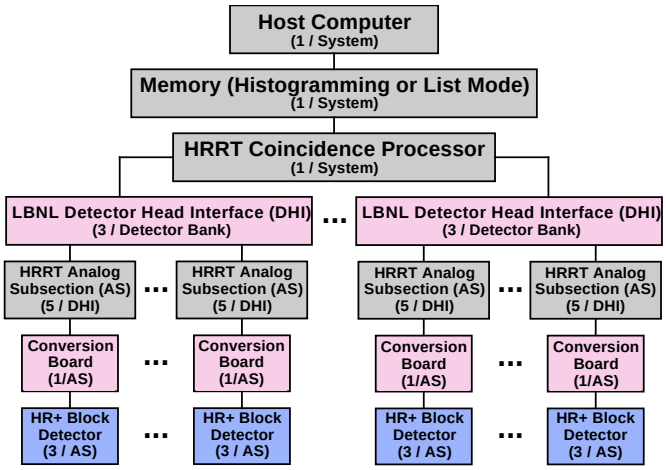

Fig. 3: Diagram of the complete data collection chain, showing the custom LBNL and CTI components and their inter-relations. The camera will use 80 CTI ECAT HR+ block detectors, 28 LBNL conversion boards, 28 CTI HRRT Analog Subsection boards, 6 LBNL custom Detector Head Interface boards, 1 CTI Coincidence Processor and a PC.

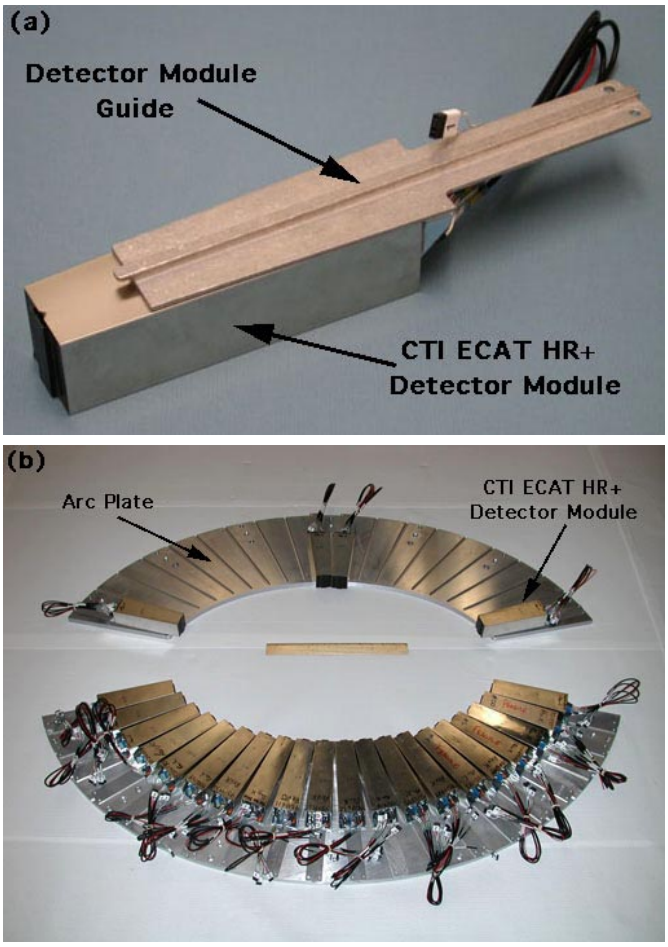

Fig. 4: (a) CTI ECAT HR+ detector module with an aluminum guide epoxied along its midline. (b) Photograph of the top and bottom aluminum arc plates with some of the CTI ECAT HR+ detector modules mounted in place. Each detector module has an aluminum guide that slides along a groove in the arc plate and is stopped (and secured against the arc plate) using a mortise and tenon. The detector modules are individually angled to point towards the center of the camera.

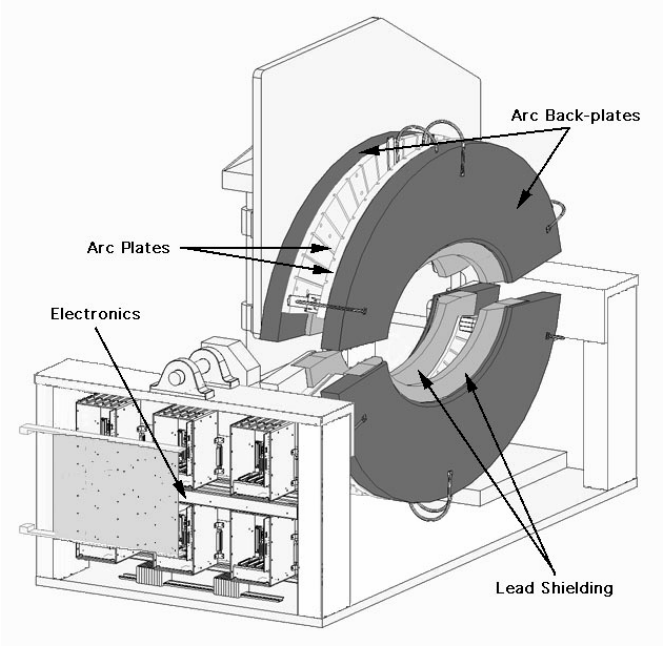

Fig. 5 3-D drawing of the prostate PET camera with some gantry details, as viewed from the side. Only a few detector modules are shown in place. The arc plates (with detector module grooves, shown in Fig. 4b) are mounted onto thicker aluminum arc back-plates that also hold the lead shielding in place. The arc plates (white), arc back-plates (dark gray) and lead shielding (light gray) are symmetric (~left and right in drawing) since there are two axial rows of detector modules. The upper bank is mounted onto a main aluminum back-plate in order to control the vertical motion using a hand-crank, allowing upward movement for patient access and downward to maximize sensitivity. A second hand-crank is used to adjust the overall tilt of both upper and lower banks. The near end of the drawing shows the electronics. The six DHI boards are mounted horizontally to the housings that hold their corresponding Analog Subsection boards. The Coincidence Processor board is mounted onto the cabinet door. The power supplies are mounted on the far end of the gantry. Most of the cabling is not shown, as well as the patient bed.

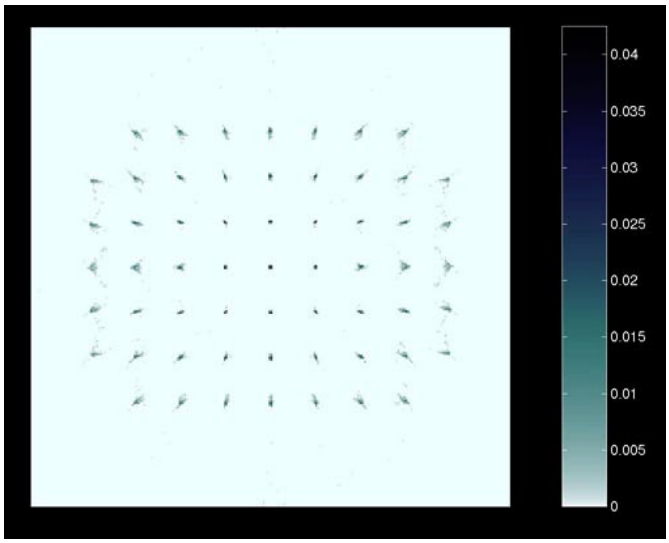

Fig. 6: Statistical noise-free reconstructed image of a point source grid when arcs are separated by the 'nominal' distance. The point sources are 5 cm apart, with the grid covering the majority of the field of view. Most point sources are located between pixels (*i.e.*, the center point source contributes to four nearby pixels). All point sources are visible (black = high uptake). Increased radial blurring is observed near the outer surface of the patient as expected due to penetration effects. However, good resolution is demonstrated in the center near the prostate, with minimal blurring in a 10 cm diameter central region. The central point has both a radial and tangential fwhm of 2 mm. The surrounding eight points have a radial fwhm of 4 mm and tangential fwhm of 3 mm. Improved resolution is expected when the reconstruction corrects for detector penetration.

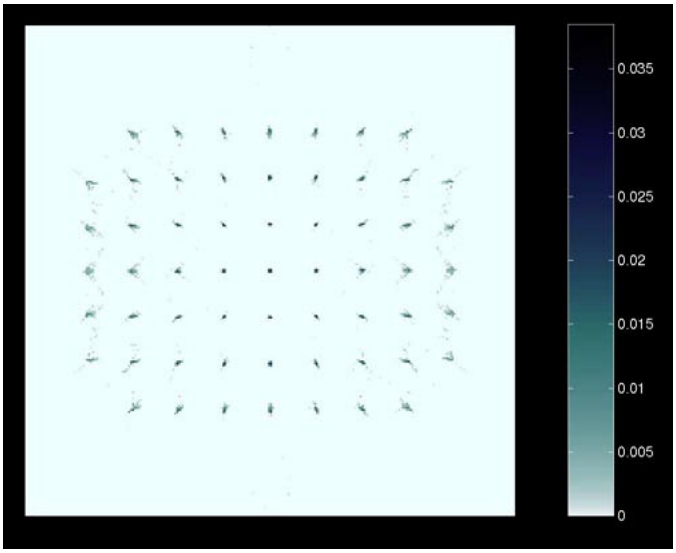

Fig. 7: Statistical noise-free reconstructed image of a point source grid when arc gap distance is increased by +5 cm from 'nominal' position. The point sources are 5 cm apart, with the grid covering the majority of the field of view. All point sources are clearly visible (black = high uptake). Good resolution is still demonstrated in the center near the prostate, with minimal blurring in a 10 cm diameter central region.

(a)

(b)

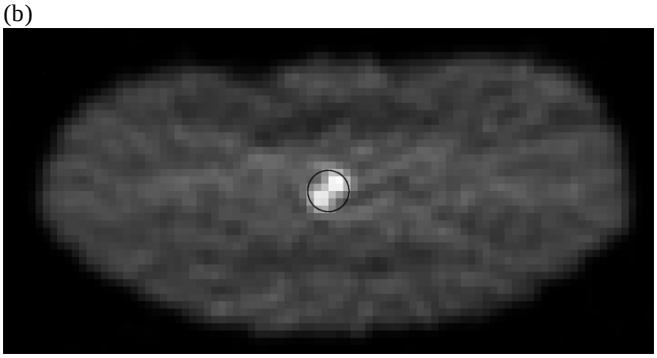

Fig. 8: (a) Body outline of patient with 2.5 cm diameter circular "prostate" divided into quadrants with "tumors" placed in the upper right and lower left quadrants (white = high uptake), assuming a tumor to background ratio of 2:1. The "patient" is 37.5 cm wide and 18.0 cm deep. (b) Reconstructed image of the phantom using an iterative maximum likelihood algorithm that assumes a 30% scatter fraction and 20% randoms fraction. Image represents 745 kcounts in a single slice, which should be achievable with a 6 minute scan after a 10 mCi injection. Both tumors are clearly visible.